Journal of Fluids Engineering. Received March 12, 2014
Accepted manuscript posted October 20, 2014. doi:10.1115/1.4028853
Copyright (c) 2014 by ASME

EULER-LAGRANGE SIMULATIONS OF BUBBLE CLOUD DYNAMICS NEAR A WALL

Jingsen Ma [1], Chao-Tsung Hsiao, and Georges L. Chahine

DYNAFLOW, INC.

www.dynaflow-inc.com

10621-J Iron Bridge Road, Jessup, MD, 20794, USA

Accepted Manuscript Not Copyedited

ABSTRACT

W*e present in this paper a two-way coupled Eulerian-Lagrangian model to study the dynamics of clouds of microbubbles subjected to pressure variations and the resulting pressures on a nearby rigid wall. The model simulates the two-phase medium as a continuum and solves the Navier-Stokes equations using Eulerian grids with a time and space varying density. The microbubbles are modeled as interacting singularities representing moving and oscillating spherical bubbles, following a modified Rayleigh-Plesset-Keller-Herring equation and are tracked in a Lagrangian fashion. A two-way coupling between the Euler and Lagrange components is realized through the local mixture density determined by the bubbles' volume change and motion. Using this numerical framework, simulations involving a large number of bubbles were conducted under driving pressures at different frequencies. The results show that the frequency of the driving pressure is critical in determining the overall dynamics: either a collective strongly coupled cluster behavior or non-synchronized weaker multiple bubble oscillations. The former creates extremely high pressures with peak values orders of magnitudes higher than that of the excitation pressure. This occurs when the driving frequency matches the natural frequency of the bubble cloud. The initial distance between the bubble cloud and the wall also affects significantly the resulting pressures. A bubble cloud collapsing very close to the wall exhibits a cascading collapse, with the bubbles farthest from the wall collapsing first and the nearest ones collapsing last, thus the energy accumulates and this results in very high pressure peaks at the wall. At farther cloud distances from the wall, the bubble cloud collapses quasi-spherically with the cloud center collapsing last.*

[1] Corresponding author, Email: jingsen@dynaflow-inc.com; Tel: +1-301-604-3688

Downloaded From: http://fluidsengineering.asmedigitalcollection.asme.org/ on 10/17/2014 Terms of Use: http://asme.org/terms

Journal of Fluids Engineering. Received March 12, 2014
Accepted manuscript posted October 20, 2014. doi:10.1115/1.4028853
Copyright (c) 2014 by ASME

KEYWORDS: Euler-Lagrange Model, Bubble Cloud Dynamics, Two-Way Coupling

INTRODUCTION

Collapse of clouds of bubbles near boundaries occur in various engineering applications such as in ultrasonic surgery [1,2], cavitating jets [3,4], unsteady sheet cavities on propeller blades [4-6], etc. Numerical modeling of this problem is challenging, since it involves bubble-bubble, bubble-flow, and bubble-wall interactions. In addition, the problem involves multi-scale physics ranging from micron-scale individual bubbles to meter- scale flow field (e.g., propeller blade). At the scale of the cloud, the interaction can be very rich since the bubbles can act in a concerted fashion collectively [7-11].

The Boundary Element Method (BEM) or Direct Numerical Simulation (DNS) which can resolve the behavior of individual bubbles provide details at several scales of interest with impressive progress reported [e.g. 11-14]. However, due to their computational cost, these methods are mostly limited to small scale problems addressed for fundamental study purposes, such as developing subgrid relationships for larger scale models. For practical applications, two-phase bubbly flows are usually modeled using one of several approaches: equivalent homogeneous continuum models, Eulerian two-fluid models, or Eulerian-Lagrangian approaches wherein the bubbles are treated as discrete particles. Homogeneous models are useful for low void fractions, whereas Eulerian-Lagrangian approaches are more appropriate for higher void fractions [12-26]. In particular, the recent work by Raju et al. [27] examined a continuum homogeneous model [28], an Eulerian multi-component model [29,30], and an Eulerian-

Accepted Manuscript Not Copyedited

Downloaded From: http://fluidsengineering.asmedigitalcollection.asme.org/ on 10/17/2014 Terms of Use: http://asme.org/terms

Journal of Fluids Engineering. Received March 12, 2014
Accepted manuscript posted October 20, 2014. doi:10.1115/1.4028853
Copyright (c) 2014 by ASME

Lagrangian model by simulating a cloud of small bubbles interacting with a large bubble oscillating in a viscous liquid. It was found that, though all the models capture the average low-frequency dynamics, the microscale response of the discrete bubbles and the resultant high-frequency local fluctuations are only captured by the Eulerian-Lagrangian solver. This highlights that a discrete bubble modeling approach is essential to a better understanding of such a problem since it can resolve the physics down to the single bubble scale, while maintaining computation cost affordable to capture the overall large scale flow behavior.

In this paper, we study the dynamics of microbubble clouds exposed to incoming pressures and the resulting pressure loads on a nearby rigid wall using a generalized 3D two-way coupled Eulerian-Lagrangian model [31,32,33]. The model simulates the two-phase medium as a continuum and solves the N-S equations with a time and space varying density, while it models the microbubbles as interacting singularities: sources representing spherical bubbles, which follow a modified Rayleigh-Plesset-Keller-Herring equation, and dipoles representing moving spheres which are tracked in a Lagrangian fashion. Non-uniformities are accounted for using surface averaged quantities (SAP model) for the bubble dynamics, in which flow quantities driving the bubble dynamics (pressures, velocities, and their gradients) are obtained through an arithmetic average of these mixture properties at the six polar points on a bubble surface. A two-way coupling between the two phases is realized through the local mixture density associated with the bubble distribution in the domain, their volume change and their motion.

Accepted Manuscript Not Copyedited

Downloaded From: http://fluidsengineering.asmedigitalcollection.asme.org/ on 10/17/2014 Terms of Use: http://asme.org/terms

Journal of Fluids Engineering. Received March 12, 2014
Accepted manuscript posted October 20, 2014. doi:10.1115/1.4028853
Copyright (c) 2014 by ASME

The 3D Eulerian-Lagrangian model employed in this study has been extensively documented and applied in our previous studies. These included the investigation of the effects of a propeller flow on bubble size distribution in water [34,35], the modeling of propeller tip vortex cavitation inception [35,36], simulation of the bubbly flow in a bubble augmented propulsor [37-39], bubble entrainment in plunging jets [40] and wave propagation in bubbly media [27,31,32,33], etc. In particular, the recent work of Raju et al. [27] systematically used the same governing equations as in this study for the mixture and the discrete bubbles and studied the effects of the two-way coupling, and compared against other methods. Below we provide a summary of the key features of the model.

Accepted Manuscript Not Copyedited

Two-Phase Flow Model Governing Equations

Continuum Homogeneous Mixture Flow Model

Following the theoretical work on dilute bubbly flows of van Wijngaarden [41,42], Commander & Prosperetti [43] and Brennen [44], etc., the overall liquid-gas mixture is treated as a continuum homogeneous mixture with its properties varying in space and time with the local volume fraction of the gas in the mixture [7,21,27,39,41-44]. The mixture density is defined as,

$$\rho_m = (1-\alpha)\rho_l + \alpha\rho_g, \tag{1}$$

where the subscripts '*l*' and '*g*' represent liquid and gas properties respectively while α is the gas volume fraction.

Downloaded From: http://fluidsengineering.asmedigitalcollection.asme.org/ on 10/17/2014 Terms of Use: http://asme.org/terms

Journal of Fluids Engineering. Received March 12, 2014
Accepted manuscript posted October 20, 2014. doi:10.1115/1.4028853
Copyright (c) 2014 by ASME

The unsteady Navier-Stokes equations for the homogeneous liquid-gas mixture are as follows:

$$\begin{aligned} \frac{\partial \rho_m}{\partial t} + \nabla \bullet \left(\rho_m \mathbf{u} \right) &= 0, \\ \frac{\partial \rho_m \mathbf{u}}{\partial t} + \nabla \bullet \rho_m \mathbf{u}\mathbf{u} &= -\nabla p + \nabla \bullet \boldsymbol{\tau}, \end{aligned} \tag{2}$$

where p is the mixture pressure [41,42], ρ_m is the mixture density, $\mathbf{u}$ its velocity, and $\boldsymbol{\tau}$ the stress tensor. The mixture viscosity in $\boldsymbol{\tau}$ is determined in the same way as in Equation (1). Other methods of obtaining the effective viscosity of the mixture have been used in the literature and are discussed in [43]. Here we select the simplified classical formulation of Equation(1).

$$\mu_m = \left(1-\alpha\right)\mu_l + \alpha\mu_g . \tag{3}$$

We underline here that Equations (2) are written for the mixture and not for the liquid. A different formulation is available in the literature, e.g. Ferrante & Elghobashi [46], Darmana et al. [47] and Shams et al. [48], and applies the Navier Stokes equations to the liquid (not the mixture) and, as a result, requires an additional momentum exchange term. Here, a separate computation of the bubble motion and of the drag force is conducted.

Bubble Motion and Volume Change

All bubbles in the two-phase mixture are tracked and both their positions and sizes are determined as functions of time. The equivalent spherical bubble radius, R(t) of each bubbles in the two-phase mixture is obtained using a modified Rayleigh-Plesset-Keller-

Accepted Manuscript Not Copyedited

Downloaded From: http://fluidsengineering.asmedigitalcollection.asme.org/ on 10/17/2014 Terms of Use: http://asme.org/terms

Journal of Fluids Engineering. Received March 12, 2014
Accepted manuscript posted October 20, 2014. doi:10.1115/1.4028853
Copyright (c) 2014 by ASME

Herring equation [5] which accounts for the surrounding medium compressibility and non-uniform pressure field [27,38,49,50]:

$$\left(1-\frac{\dot{R}}{c_m}\right)R\ddot{R}+\frac{3}{2}(1-\frac{\dot{R}}{3c_m})\dot{R}=\frac{\left(\mathbf{u}_{enc}-\mathbf{u}_b\right)^2}{4} + \frac{1}{\rho_m}\left(1+\frac{\dot{R}}{c_m}+\frac{R}{c_m}\frac{d}{dt}\right)\left[p_v+p_g-p_{enc}-\frac{2\gamma}{R}-4\mu_m\frac{\dot{R}}{R}\right]. \quad (4)$$

In the above, c_m is the local sound speed in the mixture where the bubble is located, μ_m is the medium viscosity, p_v is the liquid vapor pressure, p_{g0} is the initial gas pressure in the bubble, k is the gas polytropic constant, γ is the surface tension, and $\mathbf{u}_b$ is the bubble center velocity. A pressure term, $\rho_m\left(\mathbf{u}_{enc}-\mathbf{u}_b\right)^2/4$, due to the bubble slip velocity relative to the liquid is added and the Surface Averaged Pressure (SAP) model [49,50] is used to determine the encountered liquid quantities (subscript enc). P_{enc} and $\mathbf{u}_{enc}$ are the encountered pressures and velocities in the liquid averaged over the bubble surface. This averaging procedure is to account for non-uniform pressures and velocities along the bubble surface. The use of P_{enc} results in a major improvement over classical models, which use the pressure at the bubble center [49,50].

The bubble trajectory is obtained using the following equation of bubble motion in the liquid flow [27,38,51]:

Accepted Manuscript Not Copyedited

Downloaded From: http://fluidsengineering.asmedigitalcollection.asme.org/ on 10/17/2014 Terms of Use: http://asme.org/terms

Journal of Fluids Engineering. Received March 12, 2014
Accepted manuscript posted October 20, 2014. doi:10.1115/1.4028853
Copyright (c) 2014 by ASME

$$\frac{d\mathbf{u}_b}{dt} = -\frac{3}{\rho_l}\nabla p - 2g + \frac{3}{4}\frac{C_D}{R}(\mathbf{u}_{enc} - \mathbf{u}_b) \mid \mathbf{u}_{enc} - \mathbf{u}_b| + \frac{3}{2\pi}\frac{C_L}{R}\sqrt{\frac{\mu_l}{\rho_l}}\frac{(\mathbf{u}_{enc} - \mathbf{u}_b)\times\boldsymbol{\omega}}{\sqrt{|\boldsymbol{\omega}|}} + \frac{3}{R}(\mathbf{u}_{enc} - \mathbf{u}_b)\dot{R}, \quad (5)$$

where C_L is the bubble lift coefficient [52], $\boldsymbol{\omega}$ is the local vorticity, and C_D is the bubble drag coefficient [53] defined as a function of the bubble Reynolds number R_{eb} using:

$$C_D = \frac{24}{R_{eb}}\left(1 + 0.197{R_{eb}}^{0.63} + 2.6\times10^{-4}{R_{eb}}^{1.38}\right), \qquad R_{eb} = \frac{2\rho_l R|\ \mathbf{u}_{enc} - \mathbf{u}_b|}{\mu_l}. \quad (6)$$

Coupling between Continuum Mixture and Bubble Models

The two-way coupling between the continuum-based model and the discrete bubble model is realized by the following procedure [31,32]:

- The bubble dynamics of the individual bubbles in the flow field are controlled by the two-phase medium local properties and gradients.
- The bubble motion in the flow field is controlled by the liquid flow field
- The local properties of the mixture, void fractions, and local densities are determined by the instantaneous bubble volumes and distributions.
- The mixture flow field has an evolving space distribution of the mixture density and satisfies overall mass and momentum conservation.

Numerical Methodology

Accepted Manuscript Not Copyedited

Downloaded From: http://fluidsengineering.asmedigitalcollection.asme.org/ on 10/17/2014 Terms of Use: http://asme.org/terms

Journal of Fluids Engineering. Received March 12, 2014
Accepted manuscript posted October 20, 2014. doi:10.1115/1.4028853
Copyright (c) 2014 by ASME

To solver the above equations and Eulerian-Lagrangian two-way coupled model is used. The homogeneous mixture equations are solved in an Eulerian framework, while the bubble dynamics is solved in a Lagrangian fashion. The following numerical procedure is employed:

The mixture flow Equations (2) are solved using the artificial-compressibility method introduced in [55], where a time derivative of the pressure is added to (2) as

$$\frac{1}{\beta_c}\frac{\partial p}{\partial \tau} + \nabla\bullet\left(\rho_m \mathbf{u}\right) + \frac{\partial \rho_m}{\partial t} = 0, \tag{7}$$

where β_c is an artificial compressibility factor and τ is the pseudo-time. This is used to better couple continuity and momentum equations during the solution and to ensure through iteration satisfaction of a divergence free velocity field for a pure liquid condition (incompressible liquid). β_c is selected to obtain converged solutions with a good convergence speed. In this study, we have selected β_c = 100 for all the simulation cases.

To obtain a time-dependent solution, a Newton iterative procedure where pseudo-time stepping in τ is used at each physical time step *t,* enables one to satisfy the continuity equation. The numerical scheme uses a finite volume formulation. A first-order Euler implicit difference formula is applied to the time derivatives. The spatial differencing of the convective terms uses a flux-difference splitting scheme based on Roe's method [56] and a van Leer's MUSCL method [57] for obtaining the third-order fluxes. A second-order central differencing is used for the viscous terms. The flux Jacobians required in an implicit scheme are obtained numerically. The resulting system

Accepted Manuscript Not Copyedited

Downloaded From: http://fluidsengineering.asmedigitalcollection.asme.org/ on 10/17/2014 Terms of Use: http://asme.org/terms

Journal of Fluids Engineering. Received March 12, 2014
Accepted manuscript posted October 20, 2014. doi:10.1115/1.4028853
Copyright (c) 2014 by ASME

of algebraic equations is solved using a discretized Newton Relaxation method in which symmetric block Gauss-Seidel sub-iterations are performed before the solution is updated at each Newton interaction.

For the Lagrangian bubble model, the bubble motion and its volume variation are obtained by integrating Equations (4) and (5) through time with an explicit Runge-Kutta fourth-order scheme. The surface average quantities are obtained through an arithmetic averaging of the mixture pressures and velocities at the six polar points on a bubble surface. The liquid quantities are not readily available and for low void fractions there are approximated to be those of the mixture properties. These mixture quantities are interpolated from the mixture flow solutions in the neighboring fluid cells. The two-way coupling between Eulerian and Lagrangian is achieved through the void fraction, which is deduced from the instantaneous bubble sizes and locations. In our previous studies, the void fraction was obtained by dividing in each computational cell the total volume of the bubbles in the cell by the total cell volume. We have found that scheme not totally satisfactory because of the requirement of the presence of many bubbles in each cell and mainly because of the non-continuous character of the void fraction across cells obtained in this way resulting in difficulties with differentiation [27,37]. To smooth the discontinuities and improve stability, we implemented a Gaussian distribution scheme to smoothly "spread" each bubble's volume over a selected radius including over neighboring cells. This scheme has been found to significantly increase numerical stability and enables the handling of high-void bubbly flow simulations [31,32,33]. This is illustrated in Fig. 1. The void fraction is obtained using the following expression:

Accepted Manuscript Not Copyedited

Downloaded From: http://fluidsengineering.asmedigitalcollection.asme.org/ on 10/17/2014 Terms of Use: http://asme.org/terms

Journal of Fluids Engineering. Received March 12, 2014
Accepted manuscript posted October 20, 2014. doi:10.1115/1.4028853
Copyright (c) 2014 by ASME

$$\alpha_i = \sum_{j=1}^{N_i} \frac{v_{i,j} V_j^b}{\sum_{k}^{N_{cells}} v_{k,j} V_k^{cell}}, \tag{8}$$

where V_j^b and V_k^{cell} are the volumes of bubble *j* and cell *k* respectively, N_i is the number of bubbles which are influence cell *i*. N_{cells} is the total number of cells "influenced" by a bubble . $v_{i,j}$ is the weight factor of the contribution of bubble *j* to cell *i* and is provided by the Gaussian distribution function:

$$v_{i,j} = \frac{1}{(\sqrt{2\pi} R_s)^3} e^{-\frac{d_{ij}^2}{2R_s^2}}, \tag{9}$$

where d_{ij} is the distance between bubble *j* and cell *i*, and R_s is the characteristic spreading radius (corresponding to the standard deviation in the Gaussian function). Since the value of Gaussian function drops to almost zero at four times the standard deviation, the actual spreading radius of the bubble volume contribution is 4 R_s.

PROBLEM SETUP

As illustrated in Fig. 2 a cloud of bubbles with an overall initial radius, A_0, driven by a pressure wave, *P(t),* is simulated. The cloud is composed of small bubbles with the same initial radii, r_{b0}. We assume that these bubbles are randomly distributed in a 3D spherical domain of radius A_0, resulting in a quasi-uniform initial void fraction distribution, α_0, within the cloud. Similar configurations were used in the past for studying the dynamics of spherical bubble clouds/clusters [4,8,11,21] under various conditions. Specifically, in this paper, we consider a cloud of bubbles with r_{b0} = 50 μm,

Accepted Manuscript Not Copyedited

Downloaded From: http://fluidsengineering.asmedigitalcollection.asme.org/ on 10/17/2014 Terms of Use: http://asme.org/terms

Journal of Fluids Engineering. Received March 12, 2014
Accepted manuscript posted October 20, 2014. doi:10.1115/1.4028853
Copyright (c) 2014 by ASME

A_0 = 1.5 mm and α_0 = 5.0 %, which is a typical configuration in cavitation erosion problems [4]. Gravity is ignored here for the sake of simplicity.

As illustrated in the recent work of Chahine et al. [54], the tuning between the cloud characteristic frequency and the pressure field frequency is essential to generating very high cavitation impulsive loads. When the frequency of the driving pressure wave matches the natural frequency of a bubble cloud, a strong collective behaviour occurs and creates extremely high pressures with peak values orders of magnitudes higher than the imposed excitation pressure. This, however, is not seen when these two frequencies do not match. Motivated by this, we consider the behavior of the bubble cloud when the surrounding pressure is forced to oscillate between 0.5 *atm* and 2 *atm*. The dynamics are compared between two frequencies: one matching the natural frequency of the cloud, ω_{cloud}, and the other one very different from this frequency. For the cases presented here, $\omega_{cloud} = 10\ kHz$. This is obtained according to the definition by Brennen [21]:

$$\omega_{cloud} = \omega_0 \left(1 + \frac{12}{\pi^2} \frac{A_0^2}{r_{b0}^2} \frac{\alpha_0}{1-\alpha_0} \right)^{-1/2}, \text{ with } \omega_0^2 = \frac{P_{amb.\max}}{\rho_l r_{b0}^2} \left(3 - \frac{2\gamma}{P_{amb.\max} r_{b0}} \right). \quad (10)$$

where $P_{amb.\max}$ = 2 *atm* is the maximal value of the imposed pressure and γ = 0.728 N/m^2 is the surface tension. As summarized below in Table 1, we show below results for a frequency of 100 *kHz* (Case 1) and 10 *kHz* (Case 2), respectively. That is to say, the driving pressure frequency in Case 2 matches the cloud frequency while that in Case 1 does not. Note, in these two cases, the bubble clouds are considered in an infinite open

Accepted Manuscript Not Copyedited

Downloaded From: http://fluidsengineering.asmedigitalcollection.asme.org/ on 10/17/2014 Terms of Use: http://asme.org/terms

Journal of Fluids Engineering. Received March 12, 2014
Accepted manuscript posted October 20, 2014. doi:10.1115/1.4028853
Copyright (c) 2014 by ASME

domain and no wall is in presence. In Case 3, the presence of the wall right at the bottom edge of the cloud (i.e., $X = -A_0$) is considered.

We discuss below the results for the three simulation cases. The comparative discussion between Cases 1 and 2 is mainly to study the effects of the frequency of the driving pressure, while that between Cases 2 and 3 is to quantify the effects of the presence of the wall.

Simulation Results & Discussion

Cloud and Bubble Dynamics

Time sequences of the bubbles location and pressures in the cloud at different times during the first cloud period are compared in Fig. 3. Cases 1, 2, and 3 are shown in columns a, b and c, respectively. The cloud period, T, is defined here as the time period between $t = 0$ and the time when the total bubble volume (i.e., the summation of the volume of all the bubbles in the cloud) reaches a minimum. The different images from top to bottom in each column correspond to different stages during the first cycle of the cloud volume oscillations. The total volume of the bubbles is displayed in Fig. 4. It is seen that overall, in all cases, the bubbles in the cloud grow and collapse in a similar way response to the driving pressure. However, the cloud behavior is very different and strongly dependent on the driving pressure frequency. When the frequency of the driving pressure wave does not match the natural frequency of the cloud (Fig. 3a), the bubbles only respond weakly by oscillating with small amplitudes. On the contrary, when the two frequencies match, the bubbles grow and collapse very violently, as

Accepted Manuscript Not Copyedited

Downloaded From: http://fluidsengineering.asmedigitalcollection.asme.org/ on 10/17/2014 Terms of Use: http://asme.org/terms

Journal of Fluids Engineering. Received March 12, 2014
Accepted manuscript posted October 20, 2014. doi:10.1115/1.4028853
Copyright (c) 2014 by ASME

evidenced by the changes of both the bubble sizes and the internal gas pressures seen in Fig. 3b and Fig. 3c. As a result, the total gas volume, i.e., the sum of the volumes of all bubbles, experiences significantly different temporal variations as shown in Fig. 4. The maximum gas volume in the case where no resonance occurs is about half that of the latter two cases, while its minimum is about double. In other words, the total gas volume sees an excursion in value that is about four times larger when the frequency of the driving pressure matches the cloud natural frequency. On the other hand, the cloud size, i.e., size of the region where the bubbles are located, does not vary much between all three cases. This is shown in Fig. 5, where the cloud radius changes during the first cycle by about 2% in Case 1 and by about 5% in Case 2 and Case 3.

It seems that, in terms of cloud volume variation, wall effects are similar to those of a single bubble near a wall. The cloud period is increased by the presence of the wall and the maximum volume is slightly reduced, as shown in Fig. 4 and Fig. 5. On the other hand, as seen when comparing Fig. 3b and Fig. 3c the presence of a rigid wall dramatically alters the order in which bubbles collapse and the amplitude of the translation motion of the bubbles. Without a wall (Case 2), the bubble cloud collapses quasi spherically with the cloud center collapsing last (Fig. 3b). On the contrary, when the bubble cloud collapses close to the wall (Case 3) a cascading effect is observed with the bubbles farthest from the wall collapsing first and the ones nearest collapsing last (Fig. 3c). Accordingly, during the collapse the gas pressures inside the bubbles far away from the wall rise up to high values earlier than those close to the wall. This is evidenced by the gas pressure variations shown by the colors in Fig. 3c (with red denoting high

Accepted Manuscript Not Copyedited

Downloaded From: http://fluidsengineering.asmedigitalcollection.asme.org/ on 10/17/2014 Terms of Use: http://asme.org/terms

Journal of Fluids Engineering. Received March 12, 2014
Accepted manuscript posted October 20, 2014. doi:10.1115/1.4028853
Copyright (c) 2014 by ASME

values and blue low values). The color change from blue to red occurs progressively from the outside edge of the cloud towards the side close to the wall. This is further illustrated in Fig. 6, which shows the distribution of the void fraction due to the bubble cloud at different instants during the first period of oscillations. Due to the selected Gaussian spreading radius of A_0 a non-zero value of the void fraction exists here, beyond the cloud radius, i.e. approximately between $-2A_0$ and $2A_0$. Also due to this large spreading radius in this example, the void fraction is not uniform inside the bubble cloud. We notice that the void fraction profiles for Case 3 (wall presence) at different times are very asymmetric especially during the collapse. In addition, during the collapse, the bubbles move towards the cloud center for Case 2, while they move towards the wall in Case 3. The bubbles speed towards the wall increases with time and a group motion with a structure similar to the reentrant jet for a single bubble develops. This interesting phenomenon is highlighted in Fig. 7, where the iso-surface of α = 5% at t = 0.9 T is shown for Case 3. This void fraction iso-surface has a very similar shape to a large bubble collapsing near a rigid wall.

Accepted Manuscript Not Copyedited

Downloaded From: http://fluidsengineering.asmedigitalcollection.asme.org/ on 10/17/2014 Terms of Use: http://asme.org/terms

Journal of Fluids Engineering. Received March 12, 2014
Accepted manuscript posted October 20, 2014. doi:10.1115/1.4028853
Copyright (c) 2014 by ASME

Bubble Size and Pressure Signals

In order to further quantify the cascading character of the collapse of the various bubbles in the cloud, the temporal variations of the radius of bubbles initially located at different positions in the cloud are compared in Fig. 8 for the three cases summarized in Table 1. The temporal size variations of three selected bubbles, all on the axis of symmetry, i.e., the x axis in above Fig. 2, are plotted: one bubble is initially located at the cloud center, $x = 0$, the second one is initially at a radial distance from the cloud center of half the initial cloud radius, $x = -A_0/2$, and the third is initially at the edge of the cloud, $x = -A_0$. It is seen that in Case 1 where the cloud and driving frequency do not correspond, the primary oscillations of all bubbles are weak and do not affect much the overall response to the imposed pressure fluctuations. Overall all three bubbles follow the same trend and reach both their maximum and minimum sizes almost simultaneously.

On the contrary, in Case 2 and Case 3 where the frequency of the driving pressures matches the natural frequency of the cloud, the bubbles collapse in a cascading fashion reaching their maximum radii each at its turn, and they then all collapse and reach their minimum values almost simultaneously. As a result, as seen from the results discussed previously, the maximum values of the bubbles inner pressures in these two cases are much larger than Case 1.

The differences between Cases 2 and 3 are consistent with what have been seen in the previous section. With the presence of the rigid wall, bubbles away from the wall

Accepted Manuscript Not Copyedited

Downloaded From: http://fluidsengineering.asmedigitalcollection.asme.org/ on 10/17/2014 Terms of Use: http://asme.org/terms

Journal of Fluids Engineering. Received March 12, 2014
Accepted manuscript posted October 20, 2014. doi:10.1115/1.4028853
Copyright (c) 2014 by ASME

begin to collapse first while the ones nearest to the wall begin their collapse last. In an infinite medium, the edge bubbles start their collapse first and the center bubbles start their collapse last. Overall, near the wall the bubbles attain a larger maximum radius, except for the bubbles very close to the wall, which are restrained by the wall presence. This can be explained by the fact that bubbles collapsing later absorb energy from those collapsing earlier and the accumulated energy causes them to overgrow and then collapse much faster.

In addition, Fig. 8c also shows high frequency oscillations of the bubble radii when the bubbles approach their maximum size. These high-frequency oscillations are amplified by the wall presence and dissipate energy stored in the bubbles. These oscillations weaken as the distance of the bubbles in the cloud from the wall increases.

Correspondingly, as shown in Fig. 9, the pressures in the cloud show very large differences between the Case 1 and the latter two cases: Case 2 and Case 3. The pressures for the first case have magnitudes very close to that of the driving pressure. However, the other two cases result in significantly larger pressure peak values. Especially, the peak created by the cloud collapsing near a wall is about an order of magnitude higher than the amplitude of the driving pressure. This is very interesting and within the expectations based on the above analysis, in particular, from Fig. 8. In Case 1, all the bubbles grow slowly and collapse weakly and the growth and collapse phases are more or less symmetric, i.e., have nearly the same durations. However, when the frequency of the driving pressures matches the natural frequency of the cloud, the cascading behavior significantly extends the phase where the total volume of the

Accepted Manuscript Not Copyedited

Downloaded From: http://fluidsengineering.asmedigitalcollection.asme.org/ on 10/17/2014 Terms of Use: http://asme.org/terms

Journal of Fluids Engineering. Received March 12, 2014
Accepted manuscript posted October 20, 2014. doi:10.1115/1.4028853
Copyright (c) 2014 by ASME

bubbles in the cloud is increasing. This causes the total volume to grow much larger than in Case 1 (see Fig. 4). On the other hand, the collapse phase is dramatically shortened, releasing all the energy previously stored into the field. For example, as seen in the bottom plot of Fig. 8, it takes more than 0.1 ms for the bubble closest to the wall to reach its maximum size but only about 0.01ms to collapse to its minimum size, r_{bmin}. What is also interesting is that the collapse of this bubble almost catches up with the bubbles starting their collapses much earlier, i.e., all reaching r_{bmin} almost simultaneously. This increases significantly the amplitude of the pressures generated. Fig. 9 also indicates that the pressures created by the cloud collapsing near the wall (Case 3), have peaks almost two times larger with a narrower time width than in Case 2. This difference could result from the fact that in Case 2 the collapse pressure wave propagates in all directions, however, in Case 3 propagation is limited by and accumulates on the wall. Another alternative explanation is that a dynamic bubble cloud near a rigid wall is equivalent to two identical clouds with a symmetry plane at the same location as the rigid wall. Therefore the pressure at the wall is practically doubled.

Accepted Manuscript Not Copyedited

Wall Effects and Pressure Impacts on the Wall

The previous sections have mainly illustrated the differences between the three test cases considered here and summarized in Table 1. As one of the major motivations of the current study is to investigate the dynamics of bubble clouds near boundaries, we will mainly focus in this section on Case 3 and analyze it further.

Downloaded From: http://fluidsengineering.asmedigitalcollection.asme.org/ on 10/17/2014 Terms of Use: http://asme.org/terms

Journal of Fluids Engineering. Received March 12, 2014
Accepted manuscript posted October 20, 2014. doi:10.1115/1.4028853
Copyright (c) 2014 by ASME

In the previous section, we have seen from Fig. 8 that the bubbles farthest from the wall start their collapse first and the ones nearest start their collapse last due to the presence of the wall. This is made further clear in Fig. 10, which plots the bubble size variations at seven locations along the axis of symmetry.

Fig. 11 shows the temporal variations of the axial velocity (*x*-component) for the seven bubbles on the axis of symmetry. The figure demonstrates well the jetting phenomenon already seen previously in Fig. 3c and Fig. 7. From Fig. 11, it is seen that during the growth phase the bubbles move away from the wall with small velocities of magnitudes about 1 m/s. However, during the collapse, the bubbles return very fast towards the wall with the center bubble having the largest maximum translation velocity of about 10 m/s. The speed then quickly slows down and reverses direction (upwards, away from the wall) during the cloud gas volume rebound due to the presence of the wall. One important observation is that the translation velocities of the bubbles while moving towards the wall are much larger than during the rebound. For instance, as seen in Fig. 11, the velocity of the center bubble is around 10 m/s when it moves towards the wall, however, it is reduced to about 1 m/s when it rebounds. This indicates that in addition to the potential energy released from the bubble collapses kinetic energy is created by the jet type flow in the cloud. These combined effects thus result in pressure peaks an order of magnitude higher than that of the imposed pressure. Fig. 12 shows the pressures measured on the wall at different radial distances from the axis. It is seen that the highest pressure at the wall is on the axis of symmetry. Off-axis the pressure decays when moving away from the axis.

Accepted Manuscript Not Copyedited

Downloaded From: http://fluidsengineering.asmedigitalcollection.asme.org/ on 10/17/2014 Terms of Use: http://asme.org/terms

Journal of Fluids Engineering. Received March 12, 2014
Accepted manuscript posted October 20, 2014. doi:10.1115/1.4028853
Copyright (c) 2014 by ASME

Summary & future work

The dynamics of a cloud of microbubbles subjected to an imposed pressure time variation and the resulting pressure loads on a nearby rigid wall are studied using a two-way coupled Euler-Lagrange model. This two-phase medium is modeled using an Eulerian continuum model while the bubbles are considered in a Lagrangian fashion. Simulations involving an initially spherical cloud of bubbles were conducted under a driving pressure field with two frequencies and with/without the presence of a rigid wall near the cloud.

The results show that the tuning between the cloud characteristic frequency and the pressure field frequency is essential to generating very high cavitation impulsive loads. When the frequency of the imposed pressure field matches the natural frequency of the overall cloud oscillation, a collective strongly coupled cluster behavior occurs, which creates very high pressures with peak values an order of magnitude larger than the excitation pressure. Otherwise, non-coupled weaker multiple bubble oscillations are seen. The presence of a wall is also critical on the resulting pressures. A bubble cloud collapsing very close to the wall exhibits a cascading collapse with the bubbles farthest away from the wall starting their collapse first and the nearest ones starting their collapse last cumulating energy and producing a large pressure peak at the wall. In absence of a wall, the bubble cloud collapses quasi spherically with the bubbles at the cloud center collapsing last. The presence of the wall results in pressure signals having peak values much higher but with a peak time duration narrower than in an infinite

Accepted Manuscript Not Copyedited

Downloaded From: http://fluidsengineering.asmedigitalcollection.asme.org/ on 10/17/2014 Terms of Use: http://asme.org/terms

Journal of Fluids Engineering. Received March 12, 2014
Accepted manuscript posted October 20, 2014. doi:10.1115/1.4028853
Copyright (c) 2014 by ASME

medium. In addition, as for a single bubble collapsing near a wall, a jet like motion forms towards the wall during the bubble cloud collapse.

It is also worthy of mention that the configuration of the cloud in this study was selected purposely to be spherical and with uniform initial sizes of microbubbles. This simplification is to facilitate the analysis and to enable comparison with previous work in the literature, which provides an analytical expression for the cloud frequency of oscillations [21]. The model as implemented and used is however fully 3D and is not configuration limited. It is also suitable for the investigation of non-spherical cloud dynamics with poly-dispersed bubble distributions, as seen in our previous studies for the modeling of cavitation on propeller blades using the natural distribution of bubble sizes in the water [34, 54]. A two-way coupled simulation of this type of problem using the present model will be an interesting extension and the subject of a future separate paper.

Accepted Manuscript Not Copyedited

ACKNOWLEDGMENTS

This work was supported by the Department of Energy under an SBIR Phase II contract DE-FG02-07ER84839. The authors would also like acknowledge support from the Office of Naval Research under contract N00014-09-C-0676 monitored by Dr. Ki-Han Kim. This work was also supported in part by grants of computer time from The National Energy Research Scientific Computing Center (NERSC), a scientific computing facility for the Office of Science in the U.S. Department of Energy.

Downloaded From: http://fluidsengineering.asmedigitalcollection.asme.org/ on 10/17/2014 Terms of Use: http://asme.org/terms

Journal of Fluids Engineering. Received March 12, 2014
Accepted manuscript posted October 20, 2014. doi:10.1115/1.4028853
Copyright (c) 2014 by ASME

NOMENCLATURE

A_0	Initial cloud radius
A	Instantaneous cloud radius
A_T	Instantaneous distance between initial cloud center and the upper edge of the cloud
A_B	Instantaneous distance between initial cloud center and the lower edge of the cloud (near the wall)
C_m	Mixture sound speed on bubble surface
C_D	Drag coefficient
C_L	Lift coefficient
d_{ij}	Distance between points *i* and *j*
k	Polytropic gas constant
Ox	Axis of symmetry
p	Pressure
p_g	Gas pressure
p_v	Vapor pressure
p_{g0}	Initial gas pressure
R	Bubble radius
R_s	Characteristic spreading radius of Gaussian void fraction scheme
r	Radial distance from axis of symmetry
r_b	Bubble radius
r_{b0}	Initial bubble radius
r_{bmax}	Maximum bubble radius
R_{eb}	Reynolds number
t	Time
T	Time period of the cloud
$\mathbf{u}$	Velocity vector
x	Axial distance from initial center of the loud
X	Distance between the center of the cloud and the wall
α	Void fraction
α_0	Initial void fraction
β_c	Artificial compressibility factor
γ	Surface tension of liquid
$\boldsymbol{\omega}$	Vorticity
ω	Imposed pressure function circular Frequency
ρ	Density
ρ_m	Density of the mixture
μ	Absolute viscosity
μ_m	Absolute viscosity of the mixture

Accepted Manuscript Not Copyedited

Downloaded From: http://fluidsengineering.asmedigitalcollection.asme.org/ on 10/17/2014 Terms of Use: http://asme.org/terms

Journal of Fluids Engineering. Received March 12, 2014
Accepted manuscript posted October 20, 2014. doi:10.1115/1.4028853
Copyright (c) 2014 by ASME

τ	Pseudo-time
$\boldsymbol{\tau}$	Stress tensor

Subscripts

0	Initial condition
b,bubble	Bubble property
cloud	Cloud property
enc	Bubble encountered mixture property
i, j, k	Indices
g	Gas property
l	Liquid property
m	Mixture property
max	Maximum
min	Minimum

REFERENCES

1. Brujan, E., Ikeda, T., Yoshinaka, K., and Matsumoto, Y., 2011, "The final stage of the collapse of a cloud of bubbles close to a rigid boundary", Ultrasonics Sonochemistry, 18(1), pp.59-64.
2. Brujan, E., Ikeda, T., and Matsumoto, Y., 2012, "Shock wave emission from a cloud of bubbles", Soft Matter, 8(21), pp.5777-5783.
3. Kalumuck, K. M., and Chahine, G. L. 2000. The use of cavitating jets to oxidize organic compounds in water. ASME J. Fluids Eng., 122(3), pp.l465-470.
4. Chahine, G.L., 2014, " Modeling of Cavitation Dynamics and Interaction with Material" Chap. 6 in "Advanced Experimental and Numerical Techniques for Cavitation Erosion Prediction", Editors K.H. Kim, G.L. Chahine, J.P. Franc, A. Karimi, Springer, V. 106, pp.123-162.

Accepted Manuscript Not Copyedited

Downloaded From: http://fluidsengineering.asmedigitalcollection.asme.org/ on 10/17/2014 Terms of Use: http://asme.org/terms

Journal of Fluids Engineering. Received March 12, 2014
Accepted manuscript posted October 20, 2014. doi:10.1115/1.4028853
Copyright (c) 2014 by ASME

5. Plesset, M.S. and Prosperetti, A., 1977, "Bubble Dynamics and Cavitation," Annual Review of Fluid Mechanics, 9, pp.145-185.
6. Blake, J. R. and Gibson, D.C., 987, “Bubble Dynamics and Cavitation”, Annual Review of Fluid Mechanics, 19 (1), pp. 99-123
7. Van Wijngaarden, L., 1964, “On the Collective Collapse of a Large Number of Gas Bubbles in Water”, Proceedings 11th International Congress of Applied Mechanics, Springer, Berlin, pp.854-861.
8. Morch, K.A., 1981, “Cavity cluster dynamics and cavitation erosion,” Proc. ASME. Cavitation and Polyphase Flow Forum, pp. 1-10.
9. Chahine, G. L., 1983, “Cloud Cavitation: Theory,” Proc. 14th Symposium on Naval Hydrodynamics, Ann Arbor, Michigan, National Academy Press, pp. 165-194.
10. Chahine, G. L. and Liu, H.-L., 1985, “A Singular Perturbation Theory of the Growth of a Bubble Cluster in a Superheated Liquid,” Journal of Fluid Mechanics, 156, pp. 257-279.
11. Chahine, G. L. and Duraiswami, R., 1992, “Dynamical Interaction in a multi-Bubble Cloud,” ASME J. Fluids Eng., 114(4), pp. 680-686.
12. Esmaeeli, A. and Tryggvason, G., 1998, "Direct numerical simulations of bubbly flows. Part 1. Low Reynolds number array”, Journal of Fluid Mechanics, 377, pp. 313-345.
13. Lu, J., Biswas, S., Tryggvason, G, 2006, “A DNS study of laminar bubbly flows in a vertical channel” International Journal of Multiphase Flow, 32, pp.643-660

Accepted Manuscript Not Copyedited

Downloaded From: http://fluidsengineering.asmedigitalcollection.asme.org/ on 10/17/2014 Terms of Use: http://asme.org/terms

Journal of Fluids Engineering. Received March 12, 2014
Accepted manuscript posted October 20, 2014. doi:10.1115/1.4028853
Copyright (c) 2014 by ASME

14. Seo, J.H, Lele, S. K., Tryggvason, G, 2010, “Investigation and modeling of bubble-bubble interaction effect in homogeneous bubbly flows”, Physics of Fluids, 22, pp. 063302
15. Crowe, C.T., Troutt, T.R. and Chung, J. N. , 1996, "Numerical Models for Two-Phase Turbulent Flows", Annual Review of Fluid Mechanics, 28, pp.11-43.
16. Balachandar, S. and Eaton, J. K., 2010, "Turbulent Dispersed Multiphase Flow", Annual Review of Fluid Mechanics, 42, pp. 111-133.
17. Apte S.V., Mahesh, K., and Lundgren, T., 2008, “Accounting for finite-size effect in disperse two-phase flow”, International Journal of Multiphase Flow, 34(3), pp. 260-271.
18. Spelt, P. D. M and A. Biesheivel, A., 1997, "On the motion of gas bubbles in homogeneous isotropic turbulence," Journal of Fluid Mechanics, 336, pp. 221-244.
19. Druzhinin, O. A. and Elghobashi,S. E. , 1998, "Direct numerical simulations of bubble-laden turbulent flows using the two-fluid formulation," Physics of Fluids, 10, pp. 685.
20. Bunner, B. and Tryggvason, G., 2003, “Effect of bubble deformation on the stability and properties of bubbly flows”, Journal of Fluid Mechanics, 495, pp. 77–118.
21. Brennen, C. E., 1995, Cavitation and Bubble Dynamics, Oxford University Press.
22. Prosperetti, A. , Sundaresan,S. , Pannala, S. and Zhang, D.Z., 2007, “Segregated methods for two-fluid models,” in Computational methods for multiphase flow, Cambridge University Press, pp. 320-385.

Accepted Manuscript, Not Copyedited

Downloaded From: http://fluidsengineering.asmedigitalcollection.asme.org/ on 10/17/2014 Terms of Use: http://asme.org/terms

Journal of Fluids Engineering. Received March 12, 2014
Accepted manuscript posted October 20, 2014. doi:10.1115/1.4028853
Copyright (c) 2014 by ASME

23. Ma, J., Oberai, Drew, D.A., Lahey, R.T., Jr,, and Moraga, F., 2010, “Two-Fluid Modeling of Bubbly Flows Around Surface Ships Using a Phenomenological Subgrid Air Entrainment Model.” Computers & Fluids, 39: pp. 77-86.

24. Ma, J., Oberai, A., Hyman, M., Drew, D.A., and Lahey, R.T., Jr, 2011, "Two-Fluid Modeling of Bubbly Flows around Surface Ships Using a Phenomenological Subgrid Air Entrainment Model." Computers & Fluids, 52, pp. 50-57.

25. Ma, J., Oberai, A., Drew, D.A., and Lahey, R.T., Jr, 2012, "A Two-Way Coupled Polydispersed Two-Fluid Model for the Simulation of Air Entrainment beneath a Plunging Liquid Jet." ASME J. Fluids Eng., 134(10), pp.101304

26. Xiang, M., Cheung, S., Yeoh, G., Zhang, W., and Tu, J., 2011, “On the numerical study of bubbly flow created by ventilated cavity in vertical pipe.”, Int J Multiphase Flow, 2011, 37(7), pp.756–768

27. Raju, R., Singh, S., Hsiao, C.-T. and Chahine, G. L., 2011, “Study of Pressure Wave Propagation in a Two-Phase Bubbly Mixture”, ASME J. Fluids Eng., 133, pp.121302.

28. Gilmore, F. R. , 1952, “The growth and collapse of a spherical bubble in a viscous compressible liquid,” California Institute of Technology, Hydro. Lab. Report 26-4.

29. Wardlaw, A., Jr. and Luton J.A., 2000, “Fluid-Structure Interaction for Close-in Explosions”, Shock and Vibration Journal, 7, pp.265-275.

30. Wardlaw, A., Jr., Luton J.A., Renzi, J. J. and Kiddy, K. , 2003, “Fluid-structure coupling methodology for undersea weapons”, Fluid Structure Interaction II, WIT Press, pp. 251–263.

Accepted Manuscript Not Copyedited

Downloaded From: http://fluidsengineering.asmedigitalcollection.asme.org/ on 10/17/2014 Terms of Use: http://asme.org/terms

Journal of Fluids Engineering. Received March 12, 2014
Accepted manuscript posted October 20, 2014. doi:10.1115/1.4028853
Copyright (c) 2014 by ASME

31. Ma, J., Singh, S., Hsiao, C-T., Choi, J-K. and Chahine, G.L., 2012, “Spherical Bubble Dynamics in a Bubbly Medium,” International Conference on Numerical Methods in Multiscale Flows, Philadelphia, PA , June 12-14,
32. Ma, J., Hsiao, C-T. and Chahine, G.L., “Bubble Dynamics in Bubbly Medium,” 2012, 65th Annual Meeting of the APS Division of Fluid Dynamics, San Diego, CA, 18-20 November
33. Ma, J., Chahine, G.L. and Hsiao, C-T., 2014. "Spherical Bubble Dynamics in a Bubbly Medium Using an Euler-Lagrange Model." Chemical Engineering Science, under review.
34. Hsiao, C.-T. and Chahine, G. L. 2012. “Effect of a propeller and gas diffusion on bubble nuclei distribution in a liquid”. Journal of Hydrodynamics, Ser. B, 24, pp. 809-822.
35. Hsiao, C.-T. and Chahine, G. L., 2004, “Prediction of tip vortex cavitation inception using coupled spherical and nonspherical bubble models and Navier–Stokes computations”. Journal of Marine Science and Technology, 8(3), pp. 99-108.
36. Hsiao, C.-T. and Chahine, G. 2008. “Numerical study of cavitation inception due to vortex/vortex interaction in a ducted Propulsor”. Journal of Ship Research, 52, pp. 114-123.
37. Wu, X., Choi, J.-K., Hsiao, C.-T. and Chahine, G. L. 2010. “Bubble augmented waterjet propulsion: Numerical and experimental studies”. In: Proc. 28th Symposium on Naval Hydrodynamics.

Accepted Manuscript Not Copyedited

Downloaded From: http://fluidsengineering.asmedigitalcollection.asme.org/ on 10/17/2014 Terms of Use: http://asme.org/terms

Journal of Fluids Engineering. Received March 12, 2014
Accepted manuscript posted October 20, 2014. doi:10.1115/1.4028853
Copyright (c) 2014 by ASME

38. Wu, X., Choi, J.-K., Singh, S., Hsiao, C-T, and Chahine, G. L. , 2012. “Experimental and Numerical Investigation of Bubble Augmented Waterjet Propulsion”, Journal of Hydrodynamics, 24(5), pp.635-647.
39. Singh, S., Choi, J.-K. and Chahine, G.L., 2012, “Optimum Configuration of an Expanding-Contracting-Nozzle for Thrust Enhancement by Bubble Injection”, ASME J. Fluids Eng., 134, pp. 0113011-0113018.
40. Hsiao, C. T., Wu, X., Ma, J. and Chahine, G. L. 2013. “Numerical and experimental study of bubble entrainment due to a horizontal plunging jet”. International Shipbuilding Progress, 60, pp. 435-469.
41. van Wijngaarden, L., 1968, “On the Equations of Motion for mixtures of Liquid and Gas Bubbles”, J. Fluid Mech. 33(3), pp.465-474
42. van Wijngaarden, L., 1972, “One-Dimensional Flow of Liquids Containing Small Gas Bubbles.” Annual Review of Fluid Mechanics. 4, pp.369-396
43. Commander, K. W. and Prosperetti, A. 1989, “Linear pressure waves in bubbly liquids: Comparison between theory and experiments”, J. of the Acoustical Society of America, 85, pp.732.
44. Brennen, C. E., 2005, Fundamentals of Multiphase Flows, Cambridge University Press.
45. Awad, M. M. and Muzzchka, Y. S., 2008, "Effective property models for homogeneous two phase flow," Experimental Thermal and Fluid Science, 33(1), pp. 106-113.

Accepted Manuscript Not Copyedited

Downloaded From: http://fluidsengineering.asmedigitalcollection.asme.org/ on 10/17/2014 Terms of Use: http://asme.org/terms

Journal of Fluids Engineering. Received March 12, 2014
Accepted manuscript posted October 20, 2014. doi:10.1115/1.4028853
Copyright (c) 2014 by ASME

46. Ferrante, A., and Elghobashi, S., 2004, "On the physical mechanisms of drag reduction in a spatially developing turbulent boundary layer laden with microbubbles," Journal of Fluid Mechanics, 503, pp. 345-355.
47. Darmana, D., Deen, N. G. and Kuipers, J. A. M., 2006, "Parallelization of an Euler-Lagrange model using mixed domain decomposition and a mirror domain technique: Application to disperse gas-liquid two-phase flow," Journal of Computational Physics, 220, pp.216–248.
48. Shams, E., Finn, J., and Apte, S. V., 2011, "A numerical scheme for Euler–Lagrange simulation of bubbly flows in complex systems". International Journal for Numerical Methods in Fluids, 67(12), pp.1865-1898.
49. Chahine, G. L., 2009, "Numerical Simulation of Bubble Flow Interactions", Journal of Hydrodynamics, Vol. 21 (3), pp 316-332.
50. Hsiao, C.-T., Chahine, G. L. and Liu, H.-L. , 2003, "Scaling Effects on Prediction of Cavitation Inception in a Line Vortex Flow", ASME J. Fluids Eng., 125, pp.53-60.
51. Johnson, V.E. and Hsieh, T. , 1966, "The Influence of the Trajectories of Gas Nuclei on Cavitation Inception," Sixth Symposium on Naval Hydrodynamics, pp. 163-179.
52. Saffman, P., 1965, "The lift on a small sphere in a slow shear flow". Journal of Fluid Mechanics, 22(02), pp. 385-400.
53. Haberman, W.L. and Morton, R.K., 1953, "An Experimental Investigation of the Drag and Shape of Air Bubbles Rising in Various Liquids," Report 802, DTMB.
54. Chahine, G.L., Hsiao, C.-T., Raju, R., 2014, "Scaling of Cavitation Bubble Cloud Dynamics on Propellers" Chap. 15 in "Advanced Experimental and Numerical

Accepted Manuscript Not Copyedited

Downloaded From: http://fluidsengineering.asmedigitalcollection.asme.org/ on 10/17/2014 Terms of Use: http://asme.org/terms

Journal of Fluids Engineering. Received March 12, 2014
Accepted manuscript posted October 20, 2014. doi:10.1115/1.4028853
Copyright (c) 2014 by ASME

Techniques for Cavitation Erosion Prediction", Editors K.H. Kim, G.L. Chahine, J.P. Franc, A. Karimi, Springer, V. 106, pp. 345-372.

55. Chorin, A. J., 1967, "A Numerical Method for Solving Incompressible Viscous Flow Problems," Journal of Computational Physics, 2, pp. 12-26.
56. Roe, P. L., 1981, "Approximate Riemann Solvers, Parameter Vectors, and Difference Schemes," Journal of Computational Physics, 43, pp. 357-372.
57. Van Leer, B., Thomas, J.L., Roe, P.L. and Newsome, R.W., 1987, "A Comparison of Numerical Flux Formulas for the Euler and Navier-Stokes Equation," AIAA Paper No. 87-1104-CP.

Accepted Manuscript Not Copyedited

Downloaded From: http://fluidsengineering.asmedigitalcollection.asme.org/ on 10/17/2014 Terms of Use: http://asme.org/terms

Journal of Fluids Engineering. Received March 12, 2014
Accepted manuscript posted October 20, 2014. doi:10.1115/1.4028853
Copyright (c) 2014 by ASME

LIST OF TABLE CAPTIONS

Table 1: Key parameters of the three study cases shown below.

LIST OF FIGURE CAPTIONS

Fig. 1: Illustration of the void fraction computation [33].

Fig. 2: Schematic of a bubble cloud with an equivalent radius *A(t)* and distributed bubbles of radius $r_b(t)$ near a rigid wall. *Ox* is the axis of symmetry and *r* is the radial distance from the axis of symmetry. The distance between the center of the cloud and the wall is *X(t)*. $A_T(t)$ and $A_B(t)$ indicate the distances between the center of the cloud and the top and bottom of the cloud respectively. The cloud is subjected to an imposed pressure function at its edge, *P(t).*

Fig. 3: Time sequences of bubble locations and pressures in a bubble cloud excited by a pressure wave as listed in Table 1: (a) Case 1, (b) Case 2, and (c) Case 3. The bubbles are represented by spheres colored by the gas pressure inside each of them. Lengths are scaled by bubble radii in the top row corresponding to 50 μm. Velocity vectors are represented by arrows. Only velocity vectors larger than 2m/s extend beyond the bubble representation and can be seen in the snapshots. The bottom row shows only the velocity vectors on the bubbles in each case at *t = T*.

Fig. 4: Variations of the total volume of all bubbles in the cloud for the 3 cases described in Table 1.

Fig. 5: Variations of the outer cloud size for the 3 cases in Table 1. A_B and A_T are the distances from the center of the cloud to the top and bottom of the cloud as defined in Fig. 2.

Fig. 6: Void fraction distributions within the cloud at different times during the first cycle for Case 2 and Case 3, i.e., without and with a wall, α_0 = 5%, ω = 10 *kHz*. (Note that due to the selected Gaussian spreading radius of A_0 (see Eq. (9)) a non-zero value of the void fraction exists here, beyond the cloud radius, i.e. approximately between – 2 A_0 and 2 A_0.)

Fig. 7: Iso-surface of 5% void fraction at *t* = 0.9 *T* for Case 3 (presence of a wall). The arrows denote the translational velocities of the bubbles located at different locations in the cloud.

Fig. 8: Comparison of the size variation of bubbles at different cloud locations for the three different test cases described in Table 1: (Top) ω = 100 *kHz*, no wall; (Middle) ω = 10 *kHz*, no wall and (Bottom) ω = 10 *kHz*, with wall

Accepted Manuscript Not Copyedited

Downloaded From: http://fluidsengineering.asmedigitalcollection.asme.org/ on 10/17/2014 Terms of Use: http://asme.org/terms

Journal of Fluids Engineering. Received March 12, 2014
Accepted manuscript posted October 20, 2014. doi:10.1115/1.4028853
Copyright (c) 2014 by ASME

Fig. 9: Comparison of the pressures at different cloud locations for the three test cases described in Table 1: (Top) ω = 100 *kHz*, no wall; (Middle) ω = 10 *kHz*, no wall and (Bottom) ω = 10 *kHz*, with wall

Fig. 10: Size variation of bubbles on the axis of symmetry at seven radial locations in the cloud for Case 3 of α_0 = 5%, ω = 10 *kHz*, with wall. The numbers 1 to 7 on each line indicate the order in which each bubble starts to collapse. Negative values of *x* correspond to bubble locations in the lower half of the cloud closer to the wall.

Fig. 11: Variations of the axial (along *x* in Fig. 2) component of bubble translation velocity for bubble on the axis of symmetry at seven radial locations in the cloud for Case 3 of α_0 = 5%, ω = 10 *kHz*, with wall.

Fig. 12: Time evolution of the pressure at different radial locations on the wall for Case 3 of α_0 = 5%, ω = 10 *kHz*, with wall.

Accepted Manuscript Not Copyedited

Downloaded From: http://fluidsengineering.asmedigitalcollection.asme.org/ on 10/17/2014 Terms of Use: http://asme.org/terms

Journal of Fluids Engineering. Received March 12, 2014
Accepted manuscript posted October 20, 2014. doi:10.1115/1.4028853
Copyright (c) 2014 by ASME

Case	$P_{max}(atm)$	$P_{min}(atm)$	$\omega_{cloud}(kHz)$	$r_0(\mu m)$	$A_0(mm)$	α_0	$\omega(kHz)$	*Wall?*
1	2	0.5	10	50	1.5	5%	100	*No*
2	2	0.5	10	50	1.5	5%	10	*No*
3	2	0.5	10	50	1.5	5%	10	*Yes*

Table 1: Key parameters of the three study cases shown below.

Accepted Manuscript Not Copyedited

Downloaded From: http://fluidsengineering.asmedigitalcollection.asme.org/ on 10/17/2014 Terms of Use: http://asme.org/terms

Journal of Fluids Engineering. Received March 12, 2014
Accepted manuscript posted October 20, 2014. doi:10.1115/1.4028853
Copyright (c) 2014 by ASME

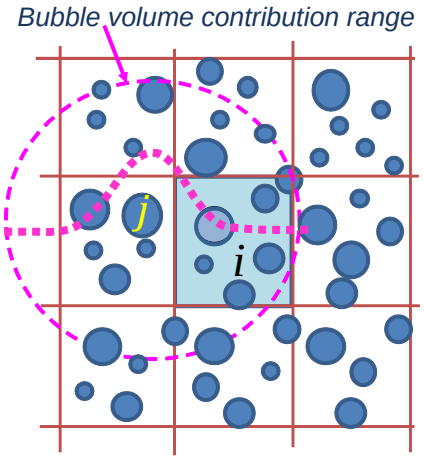

Fig. 1: Illustration of the void fraction computation [33].

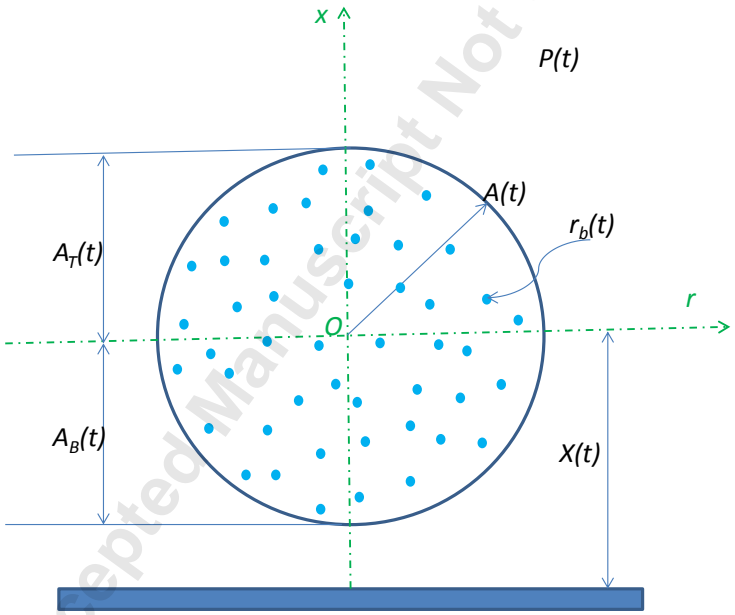

Fig. 2: Schematic of a bubble cloud with an equivalent radius *A(t)* and distributed bubbles of radius $r_b(t)$ near a rigid wall. *Ox* is the axis of symmetry and *r* is the radial distance from the axis of symmetry. The distance between the center of the cloud and the wall is *X(t)*. $A_T(t)$ and $A_B(t)$ indicate the distances between the center of the cloud and the top and bottom of the cloud respectively. The cloud is subjected to an imposed pressure function at its edge, *P(t)*.

Accepted Manuscript Not Copyedited

Downloaded From: http://fluidsengineering.asmedigitalcollection.asme.org/ on 10/17/2014 Terms of Use: http://asme.org/terms

Journal of Fluids Engineering. Received March 12, 2014
Accepted manuscript posted October 20, 2014. doi:10.1115/1.4028853
Copyright (c) 2014 by ASME

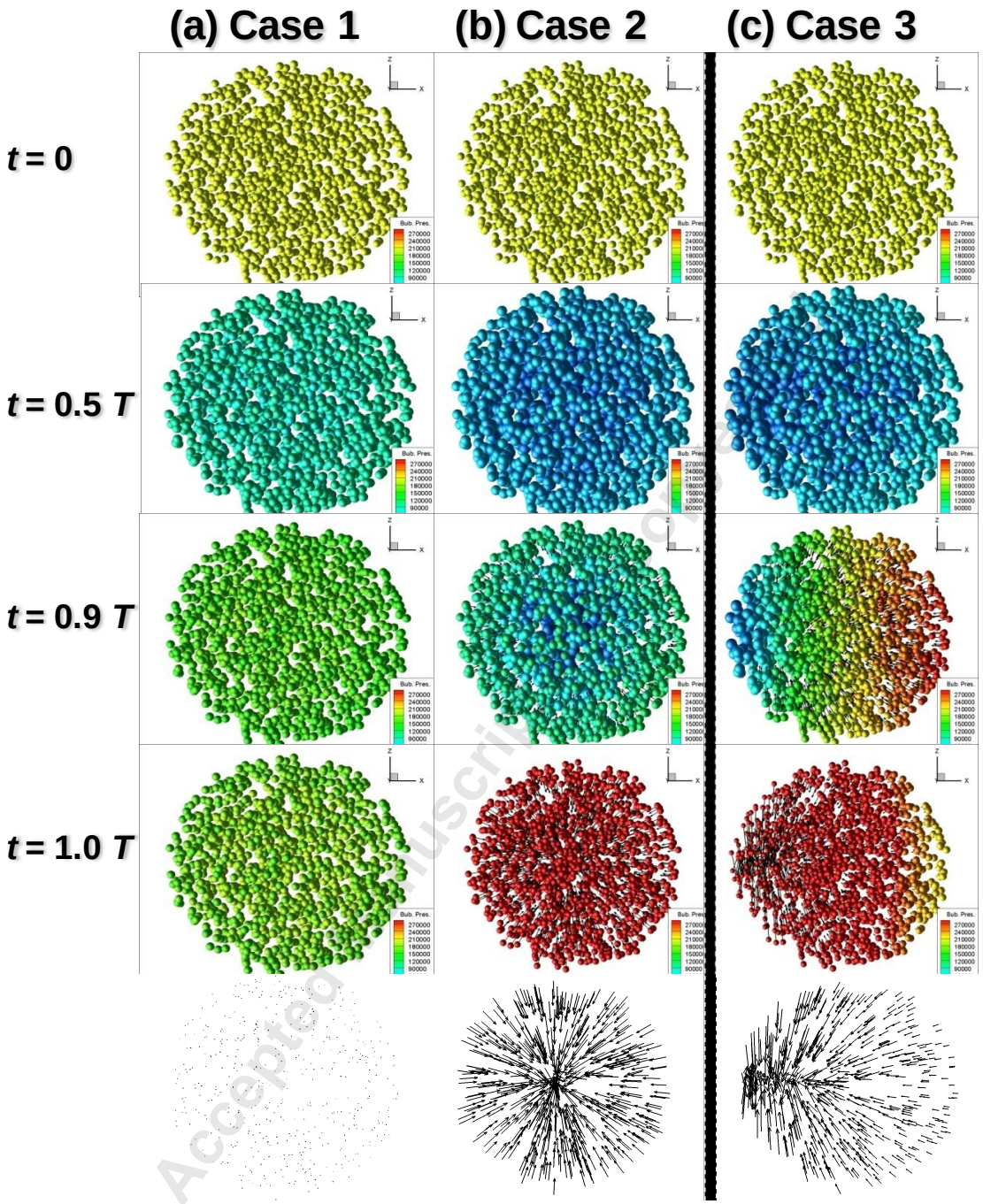

Fig. 3: Time sequences of bubble locations and pressures in a bubble cloud excited by a pressure wave as listed in Table 1: (a) Case 1, (b) Case 2, and (c) Case 3. The bubbles are represented by spheres colored by the gas pressure inside each of them. Lengths are scaled by bubble radii in the top row corresponding to 50 µm. Velocity vectors are represented by arrows. Only velocity vectors larger than 2m/s extend beyond the bubble representation and can be seen in the snapshots. The bottom row shows only the velocity vectors on the bubbles in each case at *t = T*.

Downloaded From: http://fluidsengineering.asmedigitalcollection.asme.org/ on 10/17/2014 Terms of Use: http://asme.org/terms

Journal of Fluids Engineering. Received March 12, 2014
Accepted manuscript posted October 20, 2014. doi:10.1115/1.4028853
Copyright (c) 2014 by ASME

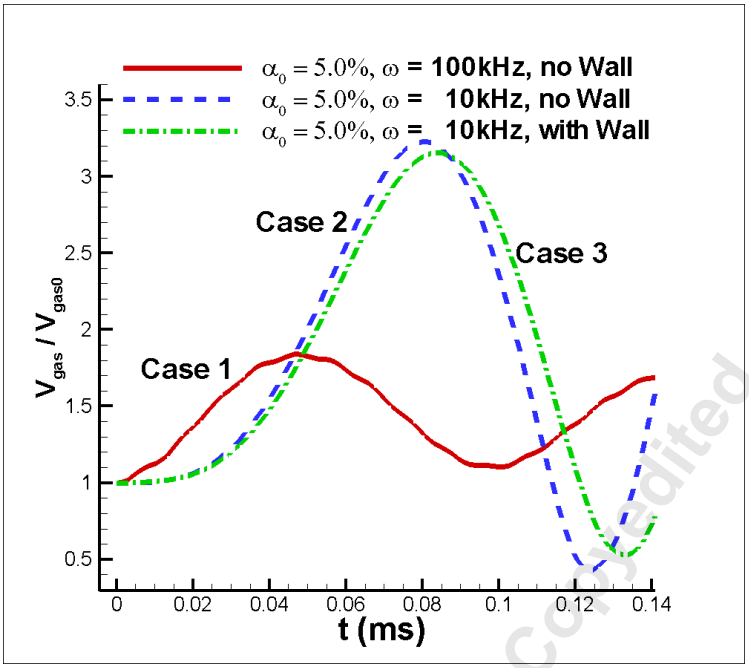

Fig. 4: Variations of the total volume of all bubbles in the cloud for the 3 cases described in Table 1.

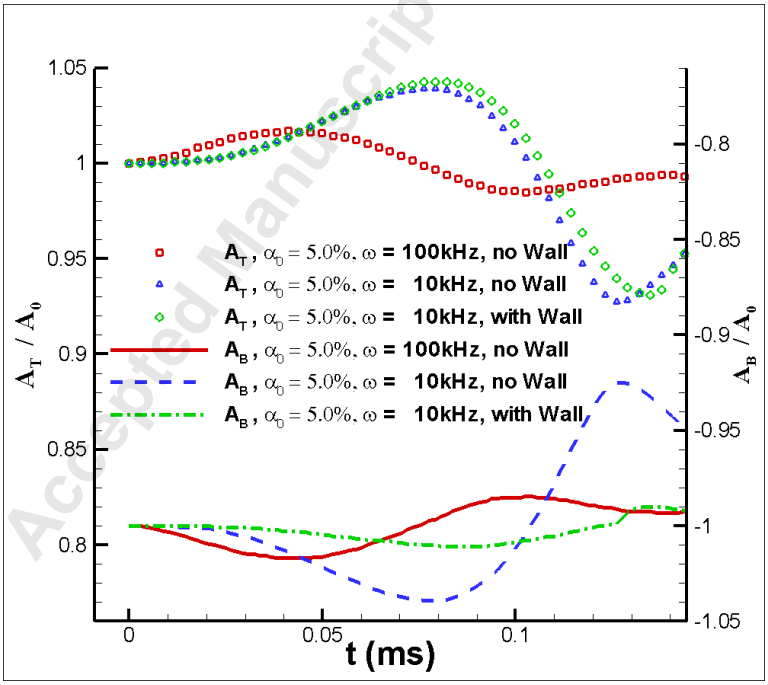

Fig. 5: Variations of the outer cloud size for the 3 cases in Table 1. A_B and A_T are the distances from the center of the cloud to the top and bottom of the cloud as defined in Fig. 2.

Downloaded From: http://fluidsengineering.asmedigitalcollection.asme.org/ on 10/17/2014 Terms of Use: http://asme.org/terms

Journal of Fluids Engineering. Received March 12, 2014
Accepted manuscript posted October 20, 2014. doi:10.1115/1.4028853
Copyright (c) 2014 by ASME

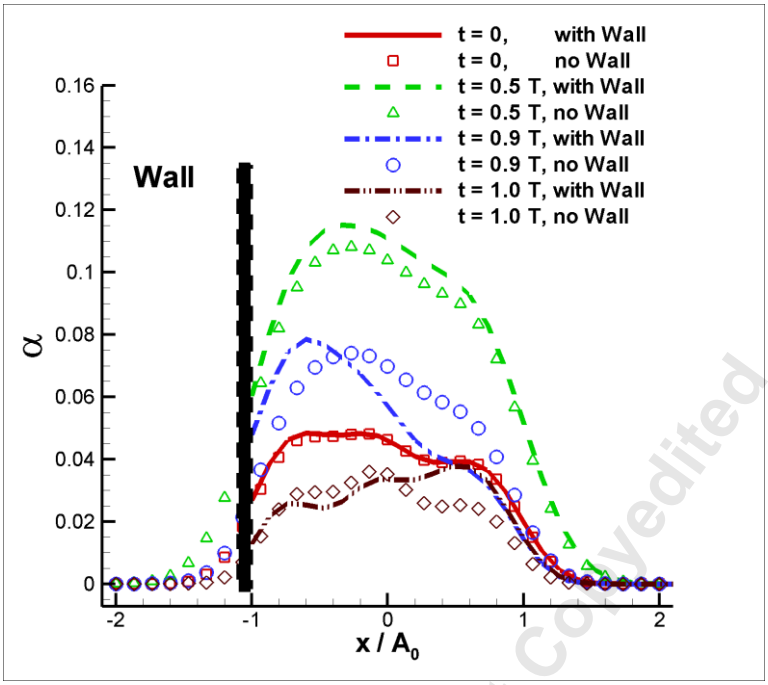

Fig. 6: Void fraction distributions within the cloud at different times during the first cycle for Case 2 and Case 3, i.e., without and with a wall, α_0 = 5%, ω = 10 *kHz*. (Note that due to the selected Gaussian spreading radius of A_0 (see Eq. (9)) a non-zero value of the void fraction exists here, beyond the cloud radius, i.e. approximately between – 2 A_0 and 2 A_0.)

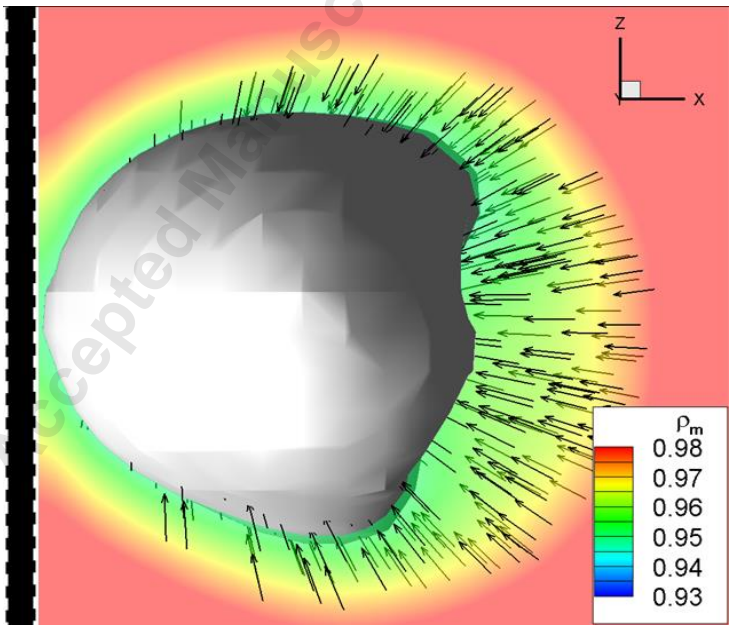

Fig. 7: Iso-surface of 5% void fraction at t = 0.9 T for Case 3 (presence of a wall). The arrows denote the translational velocities of the bubbles located at different locations in the cloud.

Downloaded From: http://fluidsengineering.asmedigitalcollection.asme.org/ on 10/17/2014 Terms of Use: http://asme.org/terms

Journal of Fluids Engineering. Received March 12, 2014
Accepted manuscript posted October 20, 2014. doi:10.1115/1.4028853
Copyright (c) 2014 by ASME

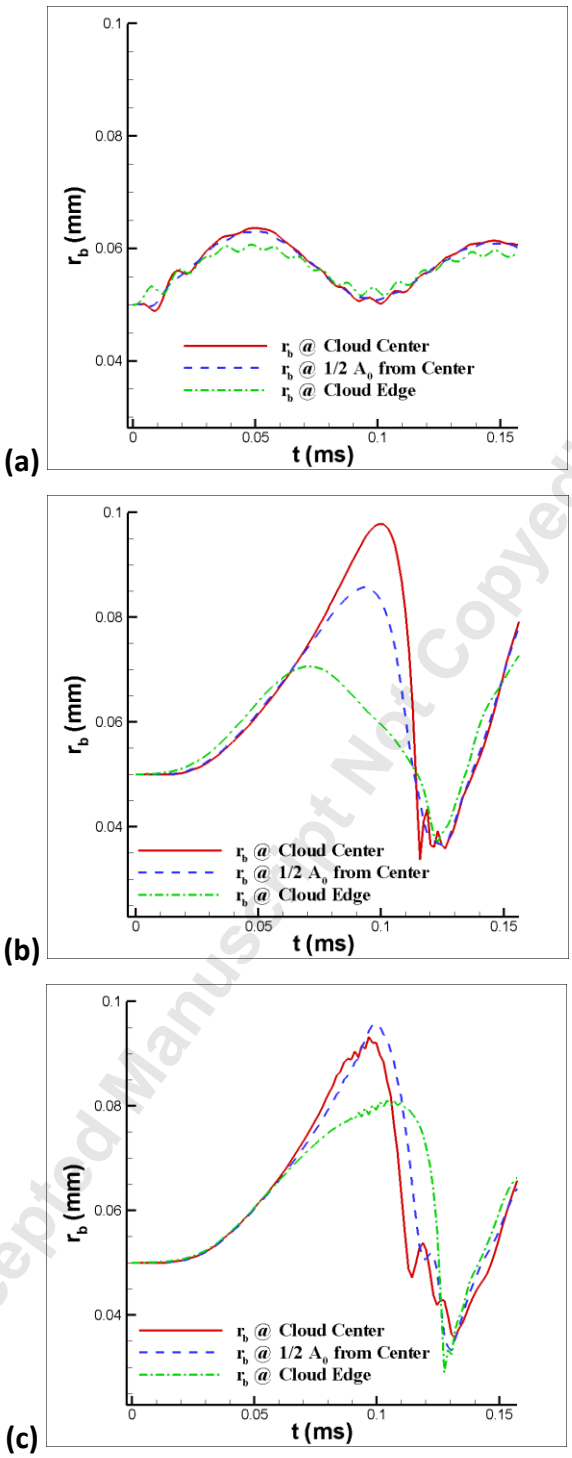

Fig. 8: Comparison of the size variation of bubbles at different cloud locations for the three different test cases described in Table 1: (Top) ω = 100 *kHz*, no wall; (Middle) ω = 10 *kHz*, no wall and (Bottom) ω = 10 *kHz*, with wall

Accepted Manuscript Not Copyedited

Downloaded From: http://fluidsengineering.asmedigitalcollection.asme.org/ on 10/17/2014 Terms of Use: http://asme.org/terms

Journal of Fluids Engineering. Received March 12, 2014
Accepted manuscript posted October 20, 2014. doi:10.1115/1.4028853
Copyright (c) 2014 by ASME

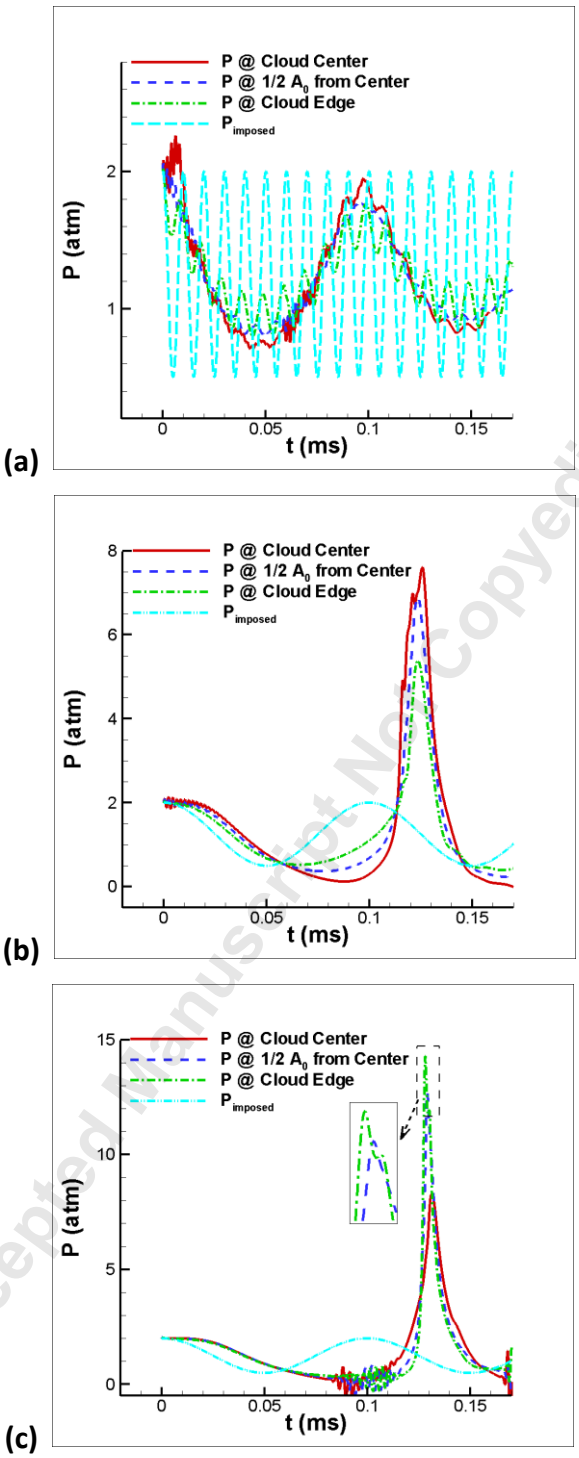

Fig. 9: Comparison of the pressures at different cloud locations for the three test cases described in Table 1: (Top) ω = 100 *kHz*, no wall; (Middle) ω = 10 *kHz*, no wall and (Bottom) ω = 10 *kHz*, with wall

Accepted Manuscript Not Copyedited

Downloaded From: http://fluidsengineering.asmedigitalcollection.asme.org/ on 10/17/2014 Terms of Use: http://asme.org/terms

Journal of Fluids Engineering. Received March 12, 2014
Accepted manuscript posted October 20, 2014. doi:10.1115/1.4028853
Copyright (c) 2014 by ASME

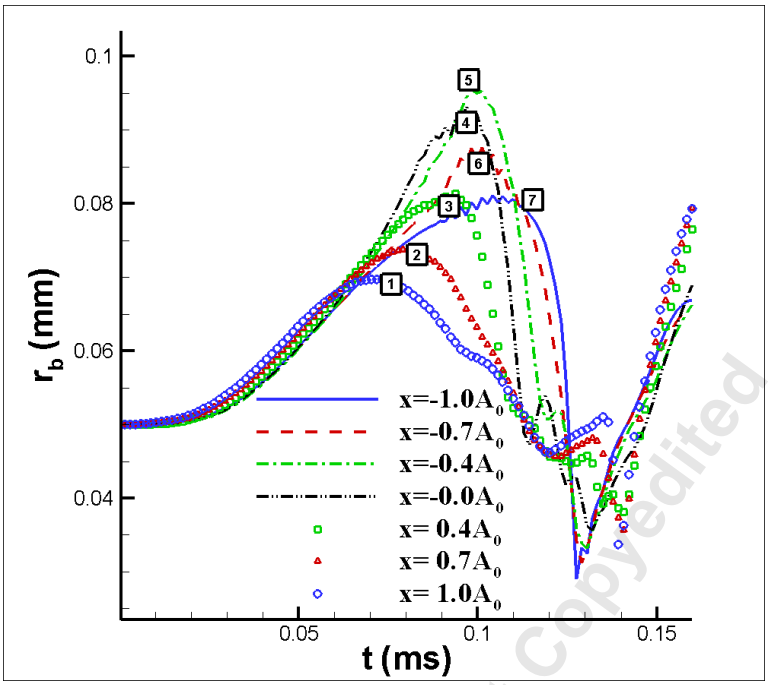

Fig. 10: Size variation of bubbles on the axis of symmetry at seven radial locations in the cloud for Case 3 of α_0 = 5%, ω = 10 *kHz*, with wall. The numbers 1 to 7 on each line indicate the order in which each bubble starts to collapse. Negative values of *x* correspond to bubble locations in the lower half of the cloud closer to the wall.

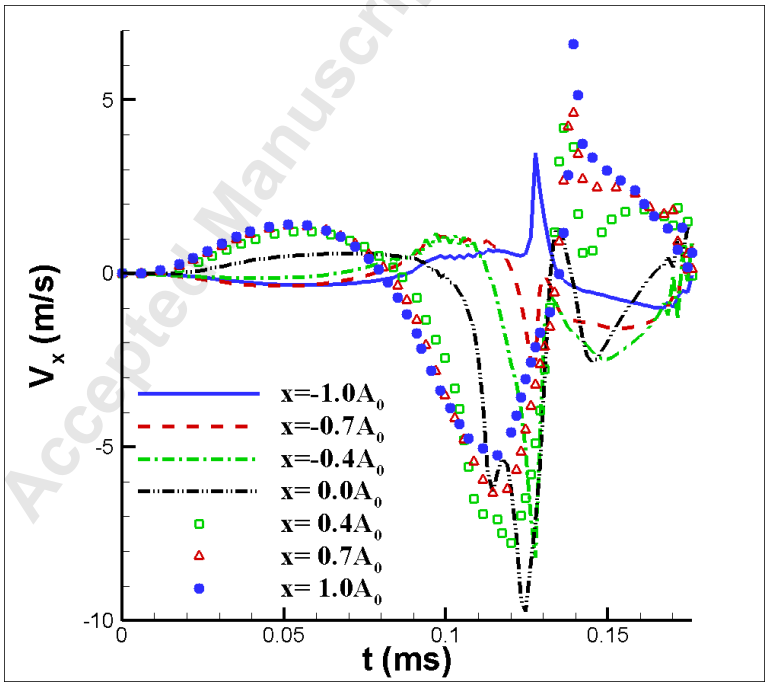

Fig. 11: Variations of the axial (along *x* in Fig. 2) component of bubble translation velocity for bubble on the axis of symmetry at seven radial locations in the cloud for Case 3 of α_0 = 5%, ω = 10 *kHz*, with wall.

Downloaded From: http://fluidsengineering.asmedigitalcollection.asme.org/ on 10/17/2014 Terms of Use: http://asme.org/terms

Journal of Fluids Engineering. Received March 12, 2014
Accepted manuscript posted October 20, 2014. doi:10.1115/1.4028853
Copyright (c) 2014 by ASME

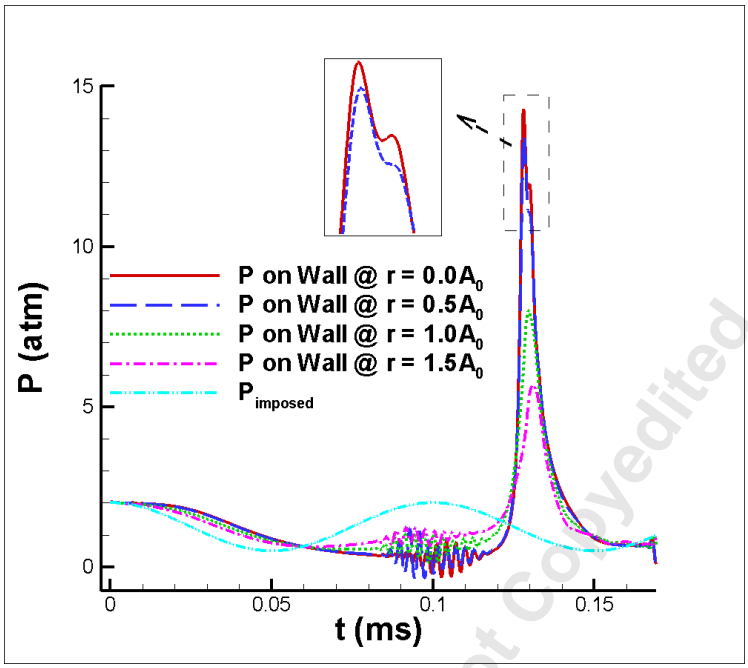

Fig. 12: Time evolution of the pressure at different radial locations on the wall for Case 3 of α_0 = 5%, ω = 10 *kHz*, with wall.

Accepted Manuscript Not Copyedited

Downloaded From: http://fluidsengineering.asmedigitalcollection.asme.org/ on 10/17/2014 Terms of Use: http://asme.org/terms